

Spectra of plasmon-exciton composite under weak coherent pumping within cavity QED treatment

Yu-Wei Lu¹ , Ling-Yan Li², Chun-Lian You² and Jing-Feng Liu²

¹ State Key Laboratory of Optoelectronic Materials and Technologies, School of Physics, Sun Yat-Sen University, Guangzhou 510275, People's Republic of China

² College of Electronic Engineering, South China Agricultural University, Guangzhou, 510642, People's Republic of China

E-mail: liujingfeng@scau.edu.cn

Received 17 September 2019, revised 13 November 2019

Accepted for publication 5 December 2019

Published 10 January 2020



CrossMark

Abstract

The quantum states of plasmon-exciton polariton are generally revealed through its scattering spectra in experiments. Here, we present the exact quantum-electrodynamics results of the spectra of plasmon-exciton composite, considering the multimode features of the plasmonic cavity. Different from a single-mode cavity, we find that the existence of higher-order modes leads to incoherent plasmon-exciton coupling, which saturates the cooperativity as the dipole moment of the quantum emitter (QE) increases. Furthermore, the competition of the coherent and incoherent coupling yields an optimal dipole moment for maximum spectral splitting. Though the higher-order modes are nonradiative, they modify the local dynamics of the QE, which present in the scattering spectra through the interplay between the dipolar plasmonic mode and the QE. We demonstrate that the scattering spectra are dominant by the cavity radiation and essentially different from the spontaneous emission (SE) spectrum. However, we show that the photoluminescence spectra of the QE coincide with its SE spectrum, which is a more reliable way to demonstrate the vacuum Rabi splitting.

Keywords: quantum plasmonics, scattering spectra, strong coupling, cQED

1. Introduction

As the efficient coherent light-matter interaction is at the heart of quantum optics and its applications, a considerable amount of attention and effort has been devoted to accessing the strong coupling regime by tailoring the local density of states (LDOS) of vacuum electromagnetic field with various materials and structures [1–5]. Among them, the plasmonic nanostructures are of great interest for recent studies that demonstrate the strong coupling between the plasmon and the single quantum emitter (QE) at room temperature [6–9]. The realization of strong coupling is often evidenced by a splitting in the scattering, absorption, and photoluminescence (PL) spectra, and these two spectral peaks are anticipated to present an avoided crossing when varying the excitation wavelength. This implies the form of dressed states between the QE and plasmon, or equally speaking, the level structures of

quasiparticle termed plasmon-exciton-polariton (PEP) [10]. In general, the Rabi oscillation is rather difficult to monitor due to the ultra-fast (fs) response of plasmonic field, and the PL spectra of the QE is also hard to observe because of the strong quenching in close proximity of metallic interface [11]; therefore, a majority of relevant experimental reports refer to the scattering or absorption spectra.

Strong coupling means the existence of coherent and reversible energy exchange between a QE and the surrounding environment, and it occurs when the coupling strength of plasmon-exciton interaction exceeds the dissipation of the hybrid system. We noticed that there is more than one definition of strong coupling in the literature, but they are based on the single mode approximation [10, 12]. Unlike the dielectric optical cavity, the plasmonic cavity modes have a low quality factor (low Q) and are concentrated [13]. The overlapping of different modes gives rise to one or more dominant

pseudomodes, whose LDOS can be much greater than the dipolar mode if the QE is close to the plasmonic structure. However, in the experimental scenarios, the QEs are designed to resonate with the dipolar mode because the higher-order modes are purely nonradiative, and, therefore, unobservable. In this case, the contribution of these nonresonant modes should not be excluded if they are not well separated from the dipolar mode. For example, previous studies have shown the effects of higher-order plasmonic modes in determining the photon statistics in weak plasmon-exciton coupling [14–16]. Intuitively, the existence of nonresonant modes not only implies that the actual coupling strength is lower than that indicated by the spectral density but also guides the energy out of the resonant mode, thereby offering additional dissipative channels for the QEs. In this sense, the evaluation of strong coupling based on the single mode approximation is ill-considered. Besides, the dynamics of the QE during SE and in the driving scheme are quite different, the physical meanings of the observable splitting in the experimental spectra should be carefully studied and clarified.

In this work, we aim to reveal the role of nonresonant modes in determining the plasmon-exciton strong coupling. We will also address the differences between the SE spectrum and the experimental scattering spectra collected from the plasmon-exciton composite illuminated by a weak coherent pump light. Based on the cavity QED (cQED) approach, we obtain the analytic expressions for the PL spectra of the QE and the scattering spectra of the plasmon-exciton composite under weak coherent pumping, which can capture the multi-mode feature of plasmonic cavity. We first demonstrate the saturation of cooperativity and the non-monotonic variation of spectral splitting as dipole moment of QE increases, resulting from the competition of the coherent and incoherent interactions between the plasmonic cavity and the QEs. Our findings are fully coincident with a recent study that is based on a semiclassical model with quasi-normal modes [17]. We have performed a detailed study on the characteristics of SE, scattering, and PL spectra, and show that the PL spectra of the QE can reveal the genuine vacuum Rabi splitting (VRS) while the scattering spectra cannot.

2. Theoretical methods

2.1. Field quantization for pseudomodes

We treat the plasmonic structure as a multimode cavity and consider that a nearby two-level QE located at \mathbf{r}_0 couples to the plasmonic cavity with transition frequency ω_0 and a dipole moment $\mathbf{d} = d\mathbf{n}$, where \mathbf{n} is the unit vector of dipole orientation. The QE dynamics is governed by the spectral density $J(\omega) = \sum_k \frac{G_k^2}{\pi} \frac{\gamma_k}{(\omega - \omega_k)^2 + (\gamma_k)^2}$, where ω_k and γ_k are the resonance frequency and decay rate of the k th plasmonic mode, respectively. $G_k = d\sqrt{\frac{\hbar\omega_k}{2\epsilon_0 V_k}} \mathbf{n} \cdot \mathbf{f}_k(\mathbf{r}_0)$ is the coupling coefficient between the quantized plasmonic eigenmodes and QE, where V_k and $\mathbf{f}_k(\mathbf{r}_0)$ are the corresponding mode volume and mode field distribution, respectively. If the plasmonic

cavity is sufficiently small, then only its dipolar mode can be excited by the incident plane wave and radiate to the far field as the dipole moment of higher-order modes are vanishing [15]. Thus, all higher-order modes remain ‘dark’ in the scattering spectra, and will be treated in the same manner. However, on the one hand, there are infinite eigenmodes in the plasmonic cavity, only several specific structures can be analytically obtained while the spectral density of the other structures must be obtained via numerical calculations. On the other hand, in general, the higher-order modes overlap each other and are irresolvable in the spectral density; thus, it is hard to extract the spectral density of a single eigenmode from its assembly. To overcome these difficulties in dealing with the plasmonic cavity, we adopt the pseudomodes method [18, 19], which replaces the numerous eigenmodes with a few pseudomodes to greatly reduce the complexity of the multi-mode problem.

In this study, we focus on the interaction between the dipolar mode and the QE. We extract the dipolar plasmonic eigenmode ($k = 1$) from the spectral density and approximate the remaining spectral density by the sum of a few Lorentz functions. Then, the spectral density can be rewritten as $J_f(\omega) = \sum_l \frac{g_l^2}{\pi} \frac{\kappa_l}{(\omega - \omega_l)^2 + (\kappa_l)^2}$, where g_l , κ_l , and ω_l are the fitting parameters obtained from the spectral density for $k \geq 2$, while $g_1 = G_1$ and $\kappa_1 = \gamma_1$. The Lorentz functions with the parameters $(\omega_l, \kappa_l, g_l)$ represent the so-called pseudomodes, which comprise one or several eigenmodes in the plasmonic cavity, i.e. the dipolar mode, quadrupolar mode, etc, while those with the parameters $(\omega_k, \gamma_k, g_k)$ correspond to the eigenmodes. Though the fitting parameters are not unique, the QE dynamics are accurate as long as the fitted spectral density is in good agreement with the original one. The pseudomodes method considerably simplifies the numerical calculations and allows for the results to fit well with the exact model.

2.2. System Hamiltonian and equations of motion

With the conception of pseudomodes, the Hamiltonian of the composite system can be written as

$$H = H_0 + H_l + H_p \quad (1)$$

with

$$H_0 = \frac{\omega_0 \sigma_z}{2} + \sum_l \omega_l a_l^\dagger a_l,$$

$$H_l = \sum_l g_l (a_l^\dagger \sigma_- + a_l \sigma_+),$$

$$H_p = \Omega_e (\sigma_+ e^{-i\omega_L t} + \sigma_- e^{i\omega_L t}) + \Omega_l (a_1^\dagger e^{-i\omega_L t} + a_1 e^{i\omega_L t}),$$

where $\sigma_z = \sigma_+ \sigma_- - \sigma_- \sigma_+$ is the inversion operator of QE, with raising and lowering operators σ_+ and σ_- , respectively. a_l is the l th quantized pseudomode with the resonance frequencies ω_l and the coupling coefficient g_l to QE. Driving Hamiltonian H_p is for the coherent pumping scheme in which ω_L is the laser frequency, $\Omega_e = \mathbf{E}_L \cdot \mathbf{d}$ and $\Omega_l = \mathbf{E}_L \cdot \boldsymbol{\mu}$ are the Rabi frequency for the QE and the l th pseudomode, respectively. $\boldsymbol{\mu}$ is the induced dipole moment of the plasmonic cavity, and \mathbf{E}_L is the intensity of the pumping field. The system dynamics follows the Liouvillian equation

$$\dot{\rho} = -i[H, \rho] + \kappa_l \mathcal{L}_{a_l}(\rho) + \frac{\gamma_n}{2} \mathcal{L}_{\sigma_z}(\rho) + \frac{\gamma_0}{2} \mathcal{L}_{\sigma_-}(\rho), \quad (2)$$

where $\mathcal{L}_{\hat{\rho}}(\rho) = 2\hat{\rho}\rho\hat{\rho}^\dagger - \{\hat{\rho}^\dagger\hat{\rho}, \rho\}$ is the Lindblad superoperator associated with the operator $\hat{\rho}$. $\mathcal{L}_{a_l}(\rho)$, $\mathcal{L}_{\sigma_z}(\rho)$, and $\mathcal{L}_{\sigma_-}(\rho)$ are the superoperators for pseudomode damping, nonradiative decays of the QE at room temperature, and radiative decays of QE, respectively. In the weak pumping regime, the population of the QE is concentrated at the ground state; thus, $\sigma_z \approx -1$ and the quantum jump term $2\hat{\rho}\rho\hat{\rho}^\dagger$ in the Lindblad superoperator can be omitted.

2.3. Spectra of plasmon-exciton composite

There are several ways to study the dynamics of a QE in a cavity. One is to monitor its PL spectra in the far field, which is obtained by taking the Fourier transform of the normally ordered correlation function of the emitted field, and expressing as $S(\omega) \propto 2 \text{Re} \left[\int_0^\infty d\tau e^{-i\omega\tau} \langle \sigma_+(t+\tau) \sigma_-(t) \rangle \right]$ [20]. Another way is to measure the steady-state scattering spectrum $I = \lim_{s \rightarrow 0^+} \int_0^\infty d\tau e^{-s\tau} \langle \mathbf{E}^-(t) \mathbf{E}^+(t+\tau) \rangle$ [21], where $\mathbf{E}^+ = \mu a_l + \mathbf{d} \sigma_-$ is the field operator at the detector. Note that the plasmonic cavity has subwavelength mode volume, i.e. is open, and hence, the field felt by the detector is the superposition of the radiation from the plasmonic cavity and the QE. The PL spectra as well as the scattering spectra are involved in the two-time correlation functions of the QE or light field, which can be calculated using the quantum regression theorem (QRT) from single-time averages if the system dynamics is Markovian [22]. A recent study has verified the validity of the QRT when the reduced time evolution of a quantum system is not Markovian, and shown the violation can happen even in some special models without non-Markovianity [23]. In our model, the initial correlations between the system and environment is absent, and the QRT is valid for any coupling strength at $t = 0$ [24]. Under the stationary condition ($t \rightarrow \infty$), the correlation function $\langle \hat{\rho}^+(t+\tau) \hat{\rho}^-(t) \rangle$ used to calculate the spectra depends only on the time difference τ [20]. Therefore, the spectra is calculated from the quantity $\langle \hat{\rho}^+(0) \hat{\rho}^-(\tau) \rangle$, which can be analytically obtained using the QRT.

From equation (2), we can obtain the evolution of the single-time averaged pseudomode operator a_l and the atomic operator σ_- in the rotating frame

$$\begin{bmatrix} \dot{\langle a_l(t) \rangle} \\ \dot{\langle \sigma_-(t) \rangle} \end{bmatrix} = -iM \begin{bmatrix} \langle a_l(t) \rangle \\ \langle \sigma_-(t) \rangle \end{bmatrix} - i \begin{bmatrix} \Omega_l \delta_{l,1} \\ \Omega_e \end{bmatrix}, \quad (3)$$

where the dot over the operators indicates the derivative with respect to time. In the above equation, $\Delta\omega_l = \omega_l - \omega_L - i\kappa_l$, $\Delta\omega_0 = \omega_0 - \omega_L - i\gamma_n$ and $\delta_{l,1}$ is the Kronecker delta. $\delta_{l,1}$ means that only the dipolar plasmonic mode is excited. The matrix M is defined as

$$M = \begin{bmatrix} \Delta\omega_l & g_l \\ \sum_l g_l & \Delta\omega_0 \end{bmatrix}. \quad (4)$$

By transforming equation (3) to the spectral domain and eliminating the nonresonant pseudomodes ($l \geq 2$) in the equation of the atom operator, we obtain

$$\langle a_l(\omega) \rangle = -\frac{i}{\omega} \frac{\frac{g_l \Omega_e}{\omega - \Delta\omega'_0} + \Omega_l}{\omega - \Delta\omega_1 - \frac{g_l^2}{\omega - \Delta\omega'_0}}, \quad (5)$$

$$\langle \sigma_-(\omega) \rangle = -\frac{i}{\omega} \frac{\frac{g_l \Omega_l}{\omega - \Delta\omega_1} - \Omega_e}{\omega - \Delta\omega'_0 - \frac{g_l^2}{\omega - \Delta\omega_1}}, \quad (6)$$

where $\Delta\omega'_0 = \omega_0 + \Delta\omega - \omega_L - i(\gamma_n + \gamma_m)$, with the modified radiative decays of QE, $\gamma_m = \sum_{l \geq 2} 2g_l^2 \frac{\kappa_l}{(\omega - \omega_l)^2 + (\kappa_l)^2}$, and the Lamb shift, $\Delta\omega = \sum_{l \geq 2} 2g_l^2 \frac{\omega - \omega_l}{(\omega - \omega_l)^2 + (\kappa_l)^2}$, induced by nonresonant pseudomodes. Unlike in the Markovian approximation [14, 15], both γ_m and $\Delta\omega$ are frequency-dependent in this case.

The QRT states that the two-time correlation functions obey the same structure as the equations describing the single-time averages. Hence, we have

$$\begin{bmatrix} \langle a_l^\dagger(t) \sigma_-(0) \rangle \\ \langle \sigma_+(t) \sigma_-(0) \rangle \end{bmatrix} = iM \begin{bmatrix} \langle a_l^\dagger(t) \sigma_-(0) \rangle \\ \langle \sigma_+(t) \sigma_-(0) \rangle \end{bmatrix} + i \begin{bmatrix} \Omega_l \delta_{l,1} \\ \Omega_e \end{bmatrix} \langle \sigma_-(0) \rangle, \quad (7)$$

$$\begin{bmatrix} \langle a_l^\dagger(t) a_l(0) \rangle \\ \langle \sigma_+(t) a_l(0) \rangle \end{bmatrix} = iM \begin{bmatrix} \langle a_l^\dagger(t) a_l(0) \rangle \\ \langle \sigma_+(t) a_l(0) \rangle \end{bmatrix} + i \begin{bmatrix} \Omega_l \delta_{l,1} \\ \Omega_e \end{bmatrix} \langle a_l(0) \rangle. \quad (8)$$

In a similar fashion as equations (5) and (6), the two-time correlation functions $\langle \sigma_+(t) \sigma_-(0) \rangle$, $\langle a_l^\dagger(t) a_l(0) \rangle$ and $\langle \sigma_+(t) a_l(0) \rangle$ can be easily solved in the S domain. A detailed deduction is provided in appendix A. As the system is initially in the ground state, the initial conditions are $\langle \sigma_+(0) \sigma_-(0) \rangle = 0$ and $\langle a_l^\dagger(0) a_l(0) \rangle = 0$. The analytical expression of the PL spectra is

$$S(\omega) \propto -\text{Im} \left[\omega \left(\omega - \Delta\omega'_0 - \sum_l \frac{g_l^2}{\omega - \Delta\omega_l} \right) \times \left(\omega + \Delta\omega_0'^* - \sum_l \frac{g_l^2}{\omega + \Delta\omega_l} \right) \right]^{-1}. \quad (9)$$

While the steady-state scattering spectra contains three parts and can be expressed as

$$I = I_{aa} + I_{a\sigma} + I_{\sigma\sigma} \quad (10)$$

with

$$I_{aa} = \left| \mu \frac{\Omega_l \Delta\omega'_0 - g_l \Omega_e}{\Delta\omega'_0 \Delta\omega_1 - g_l^2} \right|^2, \quad (11)$$

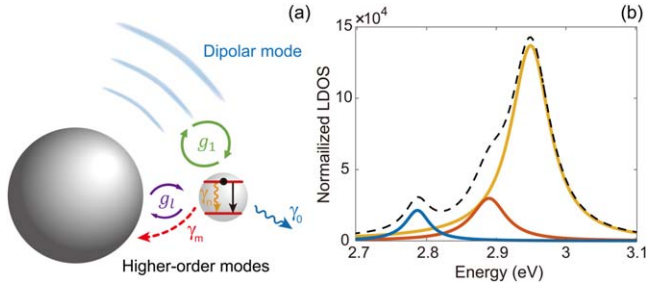


Figure 1. (a) Schematic of the hybrid system. A two-level QE couples to a plasmonic cavity and resonates with the dipolar mode. Decay rates of the excited QE, including nonradiative relaxation γ_n , radiative decay to vacuum γ_0 , and an equivalent relaxation γ_m due to the coupling to pseudomodes constituted of higher-order modes. The hybrid system is embedded in vacuum. (b) Normalized LDOS (black dashed line), the fitted dipolar mode (blue solid line), and two nonresonant pseudomodes (red and yellow solid lines) of the hybrid system.

$$I_{\sigma\sigma} = \left| \mathbf{d} \frac{\Omega_e \Delta\omega_1 - g_1 \Omega_1}{\Delta\omega'_0 \Delta\omega_1 - g_1^2} \right|^2, \quad (12)$$

$$I_{a\sigma} = 2 \operatorname{Re} \left[\mu \mathbf{d} \frac{(\Omega_1 \Delta\omega'_0 - g_1 \Omega_e)(\Omega_e \Delta\omega_1 - g_1 \Omega_1)^*}{|\Delta\omega'_0 \Delta\omega_1 - g_1^2|^2} \right]. \quad (13)$$

Note that the scattering spectra are similar to those obtained by the real space random phase approximation in [22]. However, our method is based on the cQED and goes beyond the single mode approximation. To further demonstrate the difference, we compare the scattering spectra and the PL spectra with the SE spectrum, which contains the information regarding the local dynamics of the QE. The SE spectrum $C_e(\omega)$ can be directly obtained from equation (3) with the initial conditions $\langle \sigma_+(0)\sigma_-(0) \rangle = 1$ and $\langle a_l^\dagger(0)\sigma_-(0) \rangle = 0$, which means the QE is initially in the excited state and there is no correlation between the QE and the LSP. In the absence of pumping, we can obtain

$$C_e(\omega) = -\operatorname{Im} \left[\omega - (\omega_0 - i\gamma_n) - \sum_l \frac{g_l^2}{\omega - (\omega_l - i\kappa_l)} \right]^{-1}. \quad (14)$$

The analytical expressions of various spectra (equations (9)–(14)) provided here are suitable for both weak and strong coupling, and are in good agreement with the result of numerical simulations, as we show in appendix B. Furthermore, the results can be extended to the N -QEs system, given the collective coupling strength $g_l' = \sqrt{N}g_l$ by equation (3) under the condition that the QEs are independently coupled to the plasmonic cavity without dipole–dipole interaction, as in the case of using dye molecules as QEs [6, 8].

3. Results and discussion

We use a model to illustrate our results, which is schematically shown in figure 1(a). A two-level QE is 2 nm away from the silver nanosphere. The radius of the nanosphere is $R = 8$ nm,

and the permittivity is described by the Drude model $\varepsilon_m(\omega) = \varepsilon_\infty - \omega_p^2/(\omega^2 + i\omega\gamma_p)$. The parameters are $\varepsilon_\infty = 6$, $\omega_p = 7.90$ eV, and $\gamma_p = 51$ meV [25]. The induced dipole moment of the plasmonic cavity is evaluated as $\mu = 13.6 e \cdot \text{nm}$ using the formulation $\sqrt{12\pi\hbar\eta\varepsilon_0 R^3}$, where $\eta^{-1} = d \operatorname{Re}[\varepsilon_m(\omega)]/d\varepsilon_m(\omega)|_{\omega=\omega_1}$ [16]. The dipole moment of the QE is $d = 1 e \cdot \text{nm}$ ($\approx 48 D$), with a nonradiative decay rate $\gamma_n = 20$ meV. The dipole orientation is perpendicular to the surface of the nanosphere and parallel to the polarization of the laser field. The normalized LDOS $\rho = \operatorname{Im}[\mathbf{n} \cdot \mathbf{G}(\mathbf{r}_0, \mathbf{r}_0, \omega) \cdot \mathbf{n}]/G_0$ [26], where $G_0 = (\omega/c)^3/6\pi$ is the Green's function in vacuum and calculated via the spherical Green's function [25] and shown in figure 1 (b). In the normalized LDOS, three dominant peaks can be seen, and it is well reproduced by a 3-Lorentzian fitting model with the following parameters for the spectral density: $J_f(\omega)$: $g_1 = 29.01$ meV, $g_2 = 42.95$ meV, and $g_3 = 101.7$ meV for the coupling strength between the pseudomodes and QE; $2\kappa_1 = 41.94$ meV, $2\kappa_2 = 59.14$ meV, and $2\kappa_3 = 67.90$ meV for the pseudomode damping rates; and $\omega_1 = 2.787$ eV, $\omega_2 = 2.89$ eV, and $\omega_3 = 2.95$ eV for the pseudomode resonance frequencies. We have assumed $\omega_0 = \omega_1$, unless specified otherwise. The fitting results are indicated by the solid lines in figure 1(b), from which we can clearly see that the coupling of the QE to the LSP at the QE transition frequency ω_0 (the peak location of the blue solid line) is partially supported by the nonresonant pseudomodes. We consider this part of coupling as incoherent, while the coupling of the QE to the resonant dipolar mode (blue solid line) as coherent. This model is simple but has all the features necessary to elucidate the characteristics of various spectra.

Before studying the spectra, we use specific criteria to estimate whether the composited system can be in the strong coupling regime. In strong coupling, the plasmon–exciton coupling strength exceeds the dissipation of the hybrid system, i.e. $g > (\kappa, \gamma)$, where $\gamma = \gamma_n + \gamma_m$. Then, the cooperativity $C = g_1^2/(\kappa_1\gamma)$ can be used to determine the coupling regime. Accordingly, realizing the strong light–matter interaction requires $C > 1$. Using the aforementioned parameters, we obtain $C = 1.291$, which implies that the interaction between the dipolar plasmonic mode and the QE is in the strong-coupling regime. For $g \propto d$, we note that in a single-mode cavity the cooperativity is divergent if the dipole moment of a QE increases; however, in our model, the cooperativity will not increase indefinitely, as shown in figure 2(a). As $\gamma_m \propto \sum_i g_i^2$, the cooperativity will ultimately approach $C_{\max} = g_1^2/\kappa_1\gamma_m$ if $d \rightarrow \infty$. Therefore, for a given metallic nanoparticle (MNP) and a fixed QE position, it is impossible to achieve stronger coherent coupling between plasmon and exciton beyond this bound by using a QE with a larger dipole moment. This may set a limit to some applications based on plasmonic structures. For example, it can lead to a lower bound of the spacing threshold, which is mainly determined by the cooperativity [27]. However, this topic is beyond the scope of this study.

In addition to the cooperativity, we also consider the operational definition of strong coupling, $Q = 8Ng^2/((2\kappa)^2 + \gamma^2)$, where N is the number of QEs. $Q > 1$ indicates

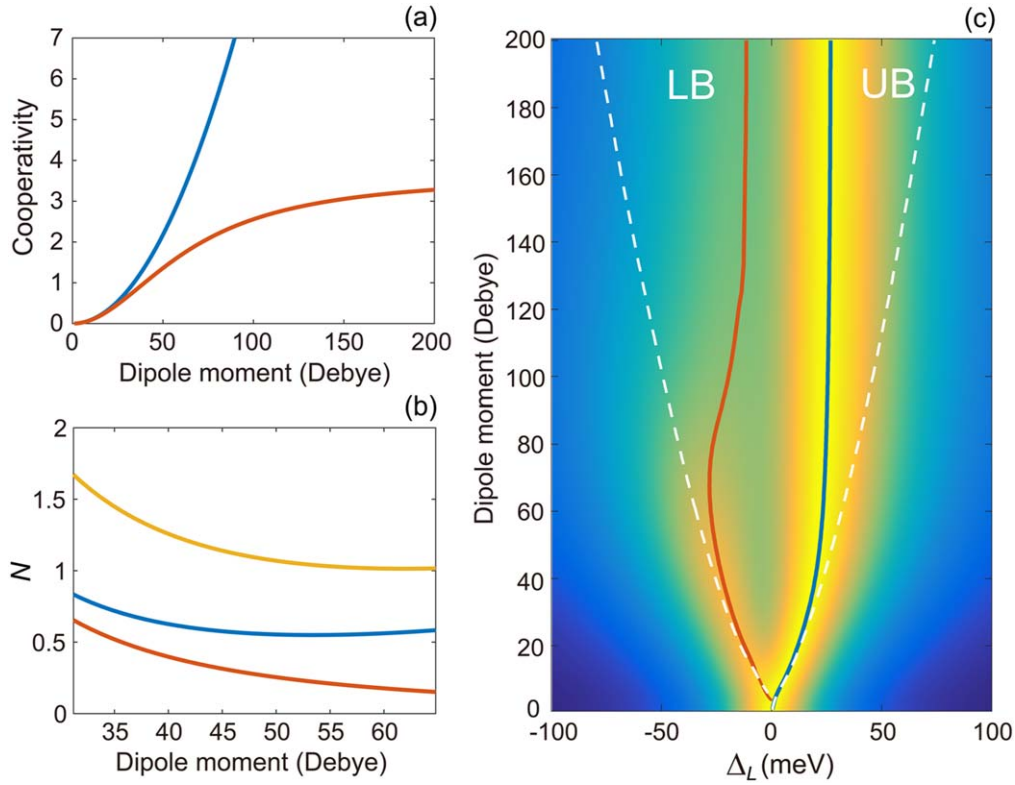


Figure 2. (a) Cooperativity of the coupling between the dipolar plasmonic mode and the QE in the single-mode case (blue line) and the exact multimode model (red line). (b) Minimum QE number N to obtain two resolvable peaks in the spectra via dipole moment. The red line indicates the single-mode case with $\gamma_n = 20$ meV, and the blue and yellow lines represent the exact multimode model with $\gamma_n = 20$ meV and $\gamma_n = 80$ meV, respectively. γ_m is frequency-dependent and can be obtained from the spectral density. (c) Normalized scattering spectrum I versus laser frequency for various dipole moments. The red and blue solid lines indicate two energy bands of PEP, and the white dashed lines show the corresponding energy bands in the single-mode case. $\Delta_L = \omega_0 - \omega_L$.

an observable splitting in the experimental spectra [8]. The required number of QEs for resolvable peaks as the function of the dipole moment is plotted in figure 2(b). We can see that the result is monotonous if the MNP is treated as a single-mode cavity ($\gamma_m = 0$, red line); while the non-monotonic variation can be observed with consideration of the non-resonant pseudomodes (blue and yellow lines denoting $\gamma_n = 20$ meV and 80 meV, respectively).

The unusual phenomena shown in figures 2(a) and (b) are due to the fact that a larger dipole moment leads to stronger coupling in both the dipolar mode and the higher-order modes, while the coupling to the latter is incoherent. This incoherent coupling induces an additional QE dissipation, γ_m , that dominates over the nonradiative relaxation and results in the saturation value of cooperativity. Therefore, a larger dipole moment does not guarantee a greater part of coherent energy exchanged between the plasmonic cavity and the QE. The competition between these two types of couplings is responsible for the non-monotonic behavior presented in figure 2(b), and the trade-off yields an optimal dipole moment for the maximum splitting in the spectra. In our model, the optimal dipole moment is around 60 D , and it increases with greater nonradiative relaxation γ_n . In figure 2(c), we plot the scattering spectra as the function of the dipole moment and the laser frequency at zero atom-cavity detuning. The upper band (UB) and lower band (LB) of the PEP are indicated by

the red and blue solid lines, respectively. We can clearly see that at first, the splitting of the two peaks becomes wider as the dipole moment increases and reaches the maximum at approximately 80 D ; then, it narrows with the continually increasing dipole moment. This behavior is distinguished from a QE interacting with a single-mode cavity, in which a larger dipole moment always produces a greater splitting, as shown by the white dashed lines.

To further verify the strong coupling, the anticrossing behavior of two bands of the PEP should be examined, and this behavior is witnessed through various spectra in the experiment. We focus on the discrepancy of the anticrossing presented in different types of spectra. Figures 3(a) and (b) show the SE spectrum and scattering spectra as the function of laser frequency, respectively. By varying the QE transition frequency, the anticrossing of the strong coupling between the dipolar plasmonic mode and the QE can be extracted from two spectra, which are shown in figure 3(c) for comparison. The anticrossings show great discrepancies from that in the single-mode case, which is shown as the black dotted lines in figure 3(c). In our model the anticrossing shows a vertical shift from $\Delta_l = 0$ due to the Lamb shift produced by the higher-order modes, which is about -80 meV as we have plotted in figure 3(d). Further, the energy (location) of the upper band is squeezed by another PEP formed by the higher-

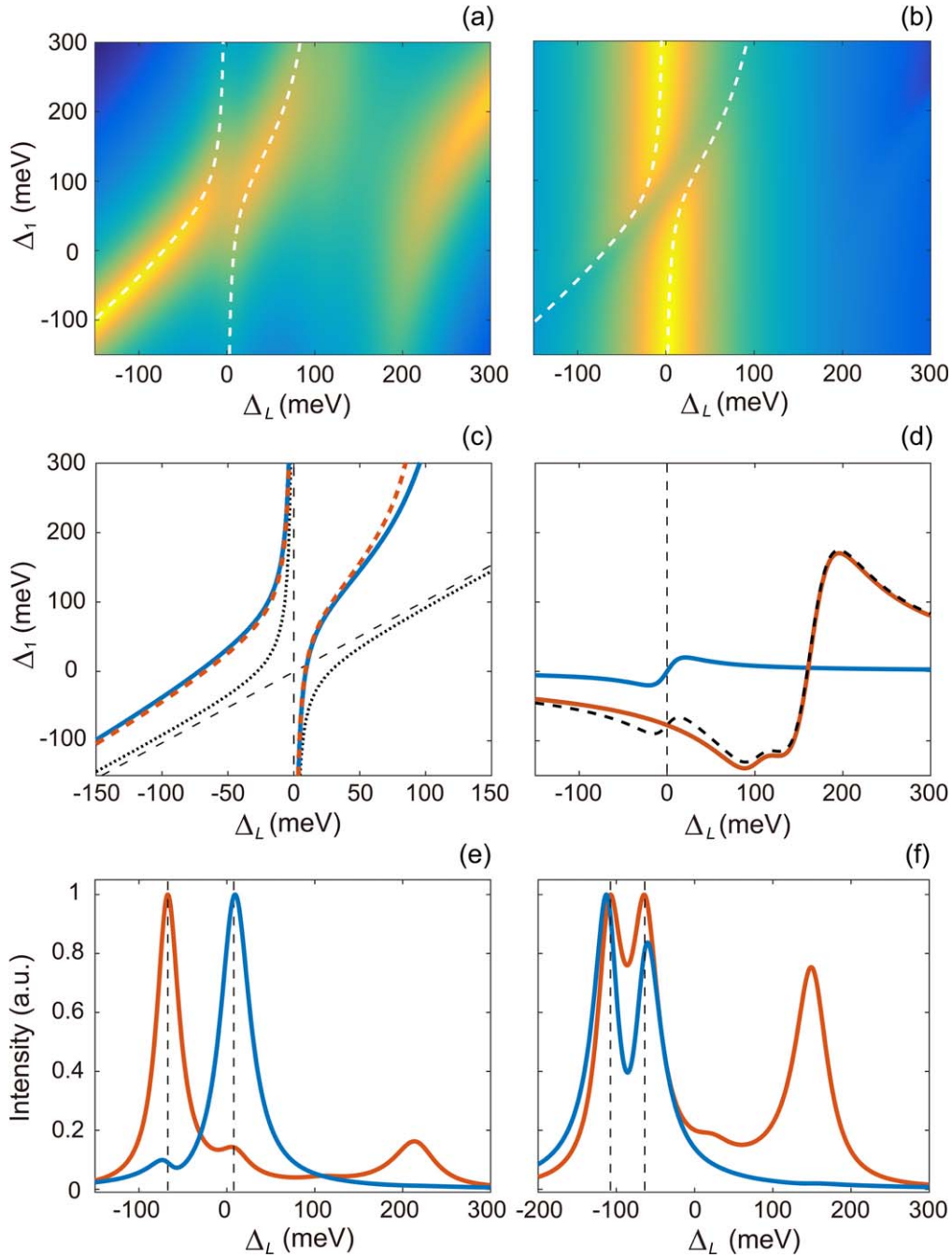


Figure 3. (a) Normalized SE spectrum $C_e(\omega)$ of the QE and (b) normalized scattering spectrum I of the plasmon-exciton composite. White dashed lines trace the spectral peaks. $\Delta_L = \omega_0 - \omega_L$, $\Delta_1 = \omega_0 - \omega_1$. (c) Anticrossing of the SE spectrum $C_e(\omega)$ (red dashed line) and scattering spectrum I (blue solid line). Two black dashed lines label the QE transition frequency ω_0 and the resonance frequency of the dipolar mode ω_1 . The black dotted lines present two bands of the PEP in the single-mode case. (d) Lamb shift (black dashed line) and the contributions of the dipolar mode (blue solid line) and higher-order modes (red solid line). The vertical dashed line labels $\Delta_L = 0$. (e) and (f) present the SE spectrum $C_e(\omega)$ (red line) and the scattering spectrum I (blue line) for $\Delta_1 = 0$ and $\Delta_1 = 88.3$ meV, respectively. The vertical dashed lines mark the position of the peaks in the SE spectrum.

order modes, whose upper band lies in 200–300 meV. This PEP can be seen in the SE spectrum (figure 3(a)) but not in the scattering spectra (figure 3(b)), because the modes are purely nonradiative. However, the QE interacts with all cavity modes and this information is encoded in the eigenfrequency of the PEP; hence, the anticrossings in the two spectra exhibit minor differences as they own the same poles, see the denominators of equations (14) and (11)–(13).

Figures 3(e) and (f) show the SE spectrum and scattering spectra for $\Delta_1 = 0$ and $\Delta_1 = 88.3$ meV (equal splitting in SE spectrum), respectively. We can see that the splittings in the scattering spectra are slightly wider, and they demonstrate a spectral shape of detuning even if the SE spectrum presents equal splitting. Therefore, the splitting in the scattering spectra cannot reflect the genuine energy level of the polaron states. Conventionally, the splitting in the SE spectrum is

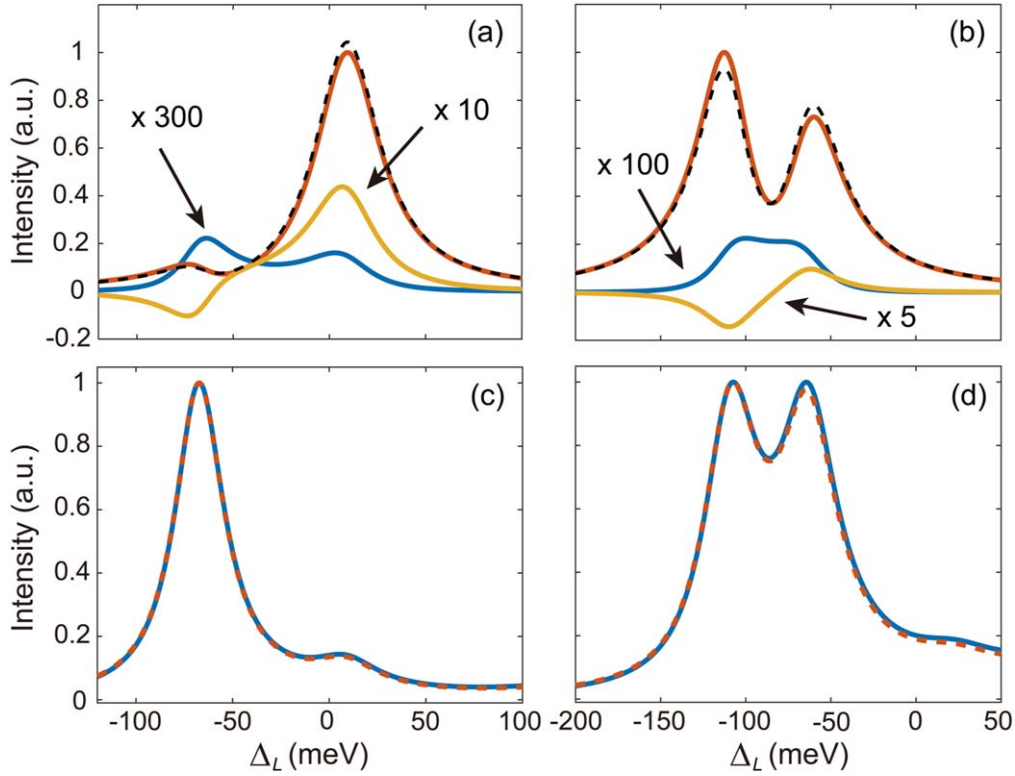


Figure 4. (a) Scattering spectra I (black dashed line) and its spectral components I_{aa} (blue solid line), $I_{\sigma\sigma}$ (red solid line) and $I_{a\sigma}$ (yellow solid line) for $\Delta_1 = 0$. (c) Normalized PL spectra $S(\omega)$ (dashed line) and SE spectrum $C_e(\omega)$ (solid line) of QE for $\Delta_1 = 0$. (b) and (d) are the same as (a) and (c), respectively, but for $\Delta_1 = 88.3$ meV.

identified as VRS; we emphasize that the splitting in the scattering spectra is not the VRS. Though the anticrossing in the scattering spectra shows minor differences compared to the SE spectrum, the underlying physical process and hence the quantum states of the system in scattering and SE are essentially different. In the scattering process, the composited system is illuminated by a probe light, and all the components in the system are excited and subsequently collected in the steady state. On the contrary, in SE, either the cavity or the QE is excited and then evolves without external driving and finally returns to the ground state. Mathematically, different ways of evolution will alter the initial conditions when applying the QRT. Considering this, we do not refer to, or consider the splitting in the scattering spectra as VRS.

A remarkable difference in the SE and scattering spectra is presented in the spectral symmetry. For example, at zero atom-cavity detuning ($\Delta_1 = 0$, figure 3(e)) the peaks in both the SE and the scattering spectra are strongly asymmetrical, but their symmetries are opposite. This feature can be seen more clearly by comparing the bright areas of the anticrossings in figures 3(a) and (b), which are complementary. This is because one energy band of the PEP is ‘cavity-like’ whereas the other is ‘atom-like.’ In the scattering spectra, the ‘cavity-like’ band is brighter for the main radiation channel of scattering is the cavity mode. While the SE spectrum is about the local dynamics of the QE, in which the intensity of the ‘atom-like’ band will be stronger.

Finally, we further discuss the characteristics of the scattering spectra. From equations (11)–(13), it can be seen

that the scattering spectra has three components I_{aa} , $I_{\sigma\sigma}$, and $I_{a\sigma}$, weighted by μ^2 , \mathbf{d}^2 , and $2\mu\mathbf{d}$, respectively. In figures 4(a) and (b), we plot each spectral component (solid lines) and the total scattering intensity (black dashed line) for $\Delta_1 = 0$ and $\Delta_1 = 88.3$ meV, respectively. We can see that the scattering spectra present distinct spectral symmetry and splitting width in different scattering channels, due to the unequal decay rates. Obviously, the scattering spectra are dominated by the scattering from cavity I_{aa} (blue line) for a large weight, while the scattering from QEs $I_{\sigma\sigma}$ (red line) are too weak to be recognized. The interaction part $I_{a\sigma}$ (yellow line), which represents the scattering from the cavity to the QE and vice versa, can be negative due to the interferences of light scattered from the cavity and the QE, which slightly enhances the spectral asymmetry. In addition, the Rabi frequency of the pumping for QE Ω_e and for the plasmonic cavity Ω_1 are not equal. These two factors are together responsible for the spectral asymmetry. Particularly, because the Rabi frequency is proportional to μ , both of these two factors originate from the large induced dipole moment μ of the plasmonic cavity. Thus, we conclude that if μ is much larger than \mathbf{d} , the scattering spectra will be nearly symmetrical. This is true for experimentally studied structures such as NPOM [6] and dimers [7]. However, the observation of VRS by pumping the plasmonic cavity is still extremely difficult because of the inevitable simultaneous excitation of the QEs by the scattering field from the plasmonic cavity. By comparing equations (9) and (14), we infer that the PL spectra of the QE will coincide with its SE spectrum, and the results are

presented in figures 4(b) and (d). Moreover, from equation (9) we can learn that the discrepancy originates from the pumping process at the beginning. Therefore, the technology of molecular electroluminescence [28] may be a potential candidate in directly uncovering the VRS in experiments of strong plasmon-exciton coupling.

4. Conclusion

We studied the role of higher-order modes in determining the characteristics of strong plasmon-exciton coupling using analytic expressions based on a multimode cQED approach. By approximating the higher-order modes via the pseudo-mode method, we showed the coupling of the QE to higher-order modes provides an additional dissipation to the QE. Therefore, an optimal dipole moment maximizes the proportions of coherent and incoherent coupling. The competitive behavior of these two types of couplings can be indirectly observed via the scattering spectra. We compared the anticrossing in the SE spectrum and the scattering spectra, and studied the characteristics of the scattering spectra in detail. The results show that the scattering spectra of the plasmon-exciton composite under the weak coherent pumping contain the information of the local dynamics of the QE; however, it is distinguished from the SE spectra obtained from an excited QE or cavity, especially in that the splitting in the scattering spectra cannot be regarded as the VRS. Furthermore, we show that the spectral symmetry of the scattering spectra is opposite to that of the SE spectrum, and it reveals the complex interaction between the dipolar mode and the QE in the scattering process by decomposing the scattering spectra into corresponding scattering channels. Finally, we show that the true VRS can be experimentally revealed via the PL spectra of the QE. Our work helps to analyze and explain the experimental results, as well as provide a better understanding of light-matter interaction in nanoscale.

Acknowledgments

This work is supported by the Fundamental Research Funds for the Central Universities (19lgyjs65), the National Natural Science Foundation of China (NSFC) (11874438, 11504115) and the Natural Science Foundation of Guangdong Province (2017A030313025).

Appendix A. Calculation of two-time correlation functions

The equations of motion of the field and atom operators are (see equation (3) in the main text)

$$\begin{aligned} \langle \dot{a}_l(t) \rangle &= -i\Delta\omega_l \langle a_l(t) \rangle - ig_l \langle \sigma_-(t) \rangle - i\Omega_l \delta_{l,1} u(t) \\ \langle \dot{\sigma}_-(t) \rangle &= -i\Delta\omega_0 \langle \sigma_-(t) \rangle - i \sum_l g_l \langle a_l(t) \rangle - i\Omega_e u(t), \end{aligned} \quad (\text{A1})$$

where $u(t)$ is the step function. Applying the Laplace transformation, in s domain we have

$$\begin{aligned} (s + i\Delta\omega_l) \langle a_l(s) \rangle &= -ig_l \langle \sigma_-(s) \rangle - i\Omega_l \delta_{l,1} \frac{1}{s} \\ (s + i\Delta\omega_0) \langle \sigma_-(s) \rangle &= -i \sum_l g_l \langle a_l(s) \rangle - i\Omega_e \frac{1}{s}. \end{aligned} \quad (\text{A2})$$

Substituting the higher-order mode ($l \geq 2$) into $\langle \sigma_-(s) \rangle$, we can obtain a set of closed equations only for dipolar mode and atom

$$\begin{aligned} (s + i\Delta\omega_1) \langle a_1(s) \rangle &= -ig_1 \langle \sigma_-(s) \rangle - i\Omega_1 \frac{1}{s} \\ (s + i\Delta\omega'_0) \langle \sigma_-(s) \rangle &= -ig_1 \langle a_1(s) \rangle - i\Omega_e \frac{1}{s}, \end{aligned} \quad (\text{A3})$$

where $\Delta\omega'_0 = \Delta\omega_0 - i \sum_{l \geq 2} \frac{g_l^2}{s + i\Delta\omega_l}$. Transforming into the frequency domain, we can find that $-i \sum_{l \geq 2} \frac{g_l^2}{s + i\Delta\omega_l} = \sum_{l \geq 2} \frac{g_l^2}{\omega - \Delta\omega_l}$ yields the modified radiative decay of QE $\gamma_m = 2 \sum_{l \geq 2} \frac{g_l^2}{(\omega - \omega_l)^2 + (\kappa_l)^2}$ and the Lamb shift $\Delta\omega = \sum_{l \geq 2} \frac{g_l^2}{(\omega - \omega_l)^2 + (\kappa_l)^2}$.

After some algebraic operations, we decouple $\langle a_1(s) \rangle$ and $\langle \sigma_-(s) \rangle$ from each other

$$\langle a_1(s) \rangle = -\frac{1}{s} \frac{\frac{g_1 \Omega_e}{s + i\Delta\omega'_0} + i\Omega_1}{s + i\Delta\omega_1 + \frac{g_1^2}{s + i\Delta\omega'_0}}, \quad (\text{A4})$$

$$\langle \sigma_-(s) \rangle = -\frac{1}{s} \frac{\frac{g_1 \Omega_1}{s + i\Delta\omega_1} + i\Omega_e}{s + i\Delta\omega'_0 + \frac{g_1^2}{s + i\Delta\omega_1}}. \quad (\text{A5})$$

Now we obtain the single-time averages that are needed for calculating the two-time correlation functions. According to QRT, the two-time correlation functions obey the same structure as the equation (A1). In order to obtain the two-time correlation function of the electric field operator $\mathbf{E}^+ = \mu a_1 + \mathbf{d}\sigma_-$, we need to calculate two sets of equations, i.e. equations (7) and (8) in the main text. We rewrite the equation (7) in here

$$\begin{aligned} \begin{bmatrix} \langle a_l^\dagger(t) \sigma_-(0) \rangle \\ \langle \sigma_+(t) \sigma_-(0) \rangle \end{bmatrix} &= iM \begin{bmatrix} \langle a_l^\dagger(t) \sigma_-(0) \rangle \\ \langle \sigma_+(t) \sigma_-(0) \rangle \end{bmatrix} \\ &+ i \begin{bmatrix} \Omega_1 \delta_{l,1} \\ \Omega_e \end{bmatrix} \langle \sigma_-(0) \rangle, \end{aligned} \quad (\text{A6})$$

where the matrix M is given by $M = \begin{bmatrix} \Delta\omega_l & g_l \\ \sum_l g_l & \Delta\omega_0 \end{bmatrix}$. Performing the Laplace transformation for above equations, we can obtain

$$\begin{aligned} (s - i\Delta\omega_l) \langle a_l^\dagger \sigma_-(s) \rangle &= ig_l \langle \sigma_+ \sigma_-(s) \rangle + i\Omega_1 \delta_{l,1} \langle \sigma_-(s) \rangle \\ (s - i\Delta\omega_0) \langle \sigma_+ \sigma_-(s) \rangle &= i \sum_l g_l \langle a_l^\dagger \sigma_-(s) \rangle + i\Omega_e \langle \sigma_-(s) \rangle. \end{aligned} \quad (\text{A7})$$

We leave the dipolar mode alone and eliminate the non-resonant pseudomodes in the second equation. Following the

similar procedure from (A1) to (A3), we can solve that

$$\langle \sigma_+ \sigma_- (s) \rangle = - \frac{\frac{g_1 \Omega_1}{s - i\Delta\omega_1} - i\Omega_e}{s - i\Delta\omega_0 + \sum_l \frac{g_l^2}{s - i\Delta\omega_l}} \langle \sigma_- (s) \rangle \quad (\text{A8})$$

$$\langle a_1^\dagger \sigma_- (s) \rangle = - \frac{\frac{g_1 \Omega_1}{s - i\Delta\omega'_0} - i\Omega_e}{s - i\Delta\omega_1 + \frac{g_1^2}{s - i\Delta\omega'_0}} \langle \sigma_- (s) \rangle. \quad (\text{A9})$$

In a similar fashion, from equation (8) in the main text we have

$$\langle a_1^\dagger a_1 (s) \rangle = - \frac{\frac{g_1 \Omega_e}{s - i\Delta\omega'_0} - i\Omega_1}{s - i\Delta\omega_1 + \frac{g_1^2}{s - i\Delta\omega'_0}} \langle a_1 (s) \rangle \quad (\text{A10})$$

$$\langle \sigma_+ a_1 (s) \rangle = - \frac{\frac{g_1 \Omega_1}{s - i\Delta\omega_1} - i\Omega_e}{s - i\Delta\omega_0 + \sum_l \frac{g_l^2}{s - i\Delta\omega_l}} \langle a_1 (s) \rangle. \quad (\text{A11})$$

With (A4) and (A5) at hand, one can obtain equation (9) by substituting s with $i\omega$ in equation (A8), and apply final value theorem to equations (A8)–(A11) to obtain equations (11)–(13) in the main text. We can see that no Markovian approximation has been made in above deduction.

Appendix B. Comparison of analytical expressions with numerical simulations

Figure B1 shows the numerical calculations of steady-state scattering spectra (equations (11)–(13)) and PL spectra (equation (14)), with the Hamilton (equation (1)) in the main text by using QuTip [29, 30] to solve the Liouvillian equation (equation (2)). In figure B2 we compare the spontaneous emission (SE) dynamics of QE (the Fourier transformation of equation (14)) calculated via the quantization of absorbing medium based on Green's tensor [31–33] and the pseudomodes method. In all simulation $\Omega_e/\kappa_1 = 0.1$, while other parameters can be found in the main text.

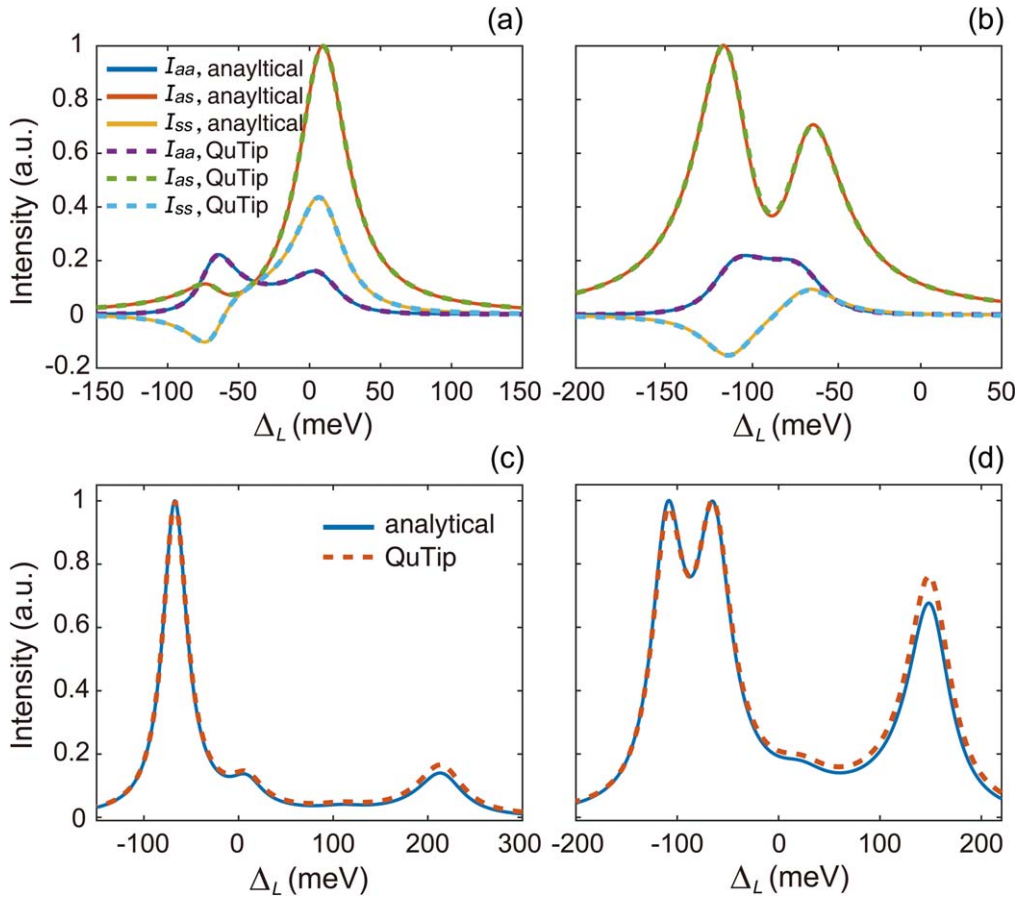


Figure B1. Comparison of the analytical expressions of spectra with numerical simulations. (a) and (b) Various spectral components for the steady-state scattering spectra. (c) and (d) Corresponding normalized PL spectra. In (a) and (c) $\Delta_1 = 0$ while $\Delta_1 = 88.3$ meV in (b) and (d). The solid lines and dashed lines are for the analytical expressions and the numerical calculations using QuTip, respectively.

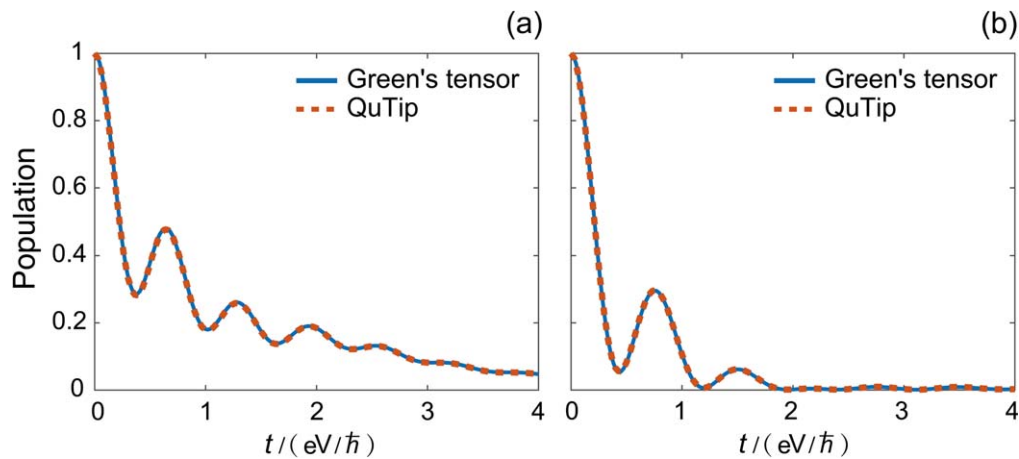


Figure B2. Comparison of the spontaneous emission dynamics of QE obtained by the quantization of absorbing medium based on Green's tensor and the numerical simulations with pseudomodes method using QuTip for (left) $\Delta_1 = 0$ and (right) $\Delta_1 = 88.3$ meV.

ORCID iDs

Yu-Wei Lu  <https://orcid.org/0000-0002-3174-6812>

References

- [1] Yoshie T, Scherer A, Hendrickson J, Khitrova G, Gibbs H, Rupper G, Ell C, Shchekin O and Deppe D 2004 *Nature* **432** 200
- [2] Rogobete L, Kaminski F, Agio M and Sandoghdar V 2007 *Opt. Lett.* **32** 1623
- [3] Pelton M 2015 *Nat. Photon.* **9** 427
- [4] Liberal I and Engheta N 2017 *Proc. Natl Acad. Sci.* **114** 822
- [5] Peng P, Liu Y C, Xu D, Cao Q T, Lu Q, Gong Q and Xiao Y F 2017 *Phys. Rev. Lett.* **119** 233901
- [6] Chikkaraddy R, De Nijs B, Benz F, Barrow S, Scherman O, Rosta E, Demetriadou A, Fox P, Hess O and Baumberg J 2016 *Nature* **535** 127
- [7] Santhosh K, Bitton O, Chuntunov L and Haran G 2016 *Nat. Commun.* **7** 11823
- [8] Liu R, Zhou Z K, Yu Y C, Zhang T, Wang H, Liu G, Wei Y, Chen H and Wang X H 2017 *Phys. Rev. Lett.* **118** 237401
- [9] Groß H, Hamm J, Tufarelli T, Hess O and Hecht B 2018 *Sci. Adv.* **4** 4906
- [10] Törmä P and Barnes W 2014 *Rep. Prog. Phys.* **78** 013901
- [11] Delga A, Feist J, Bravo-Abad J and Garcia-Vidal F 2014 *Phys. Rev. Lett.* **112** 253601
- [12] Kimble H 1998 *Phys. Scr.* **T76** 127
- [13] Li R Q, Hernández-Pérez D, García-Vidal F and Fernández-Domínguez A 2016 *Phys. Rev. Lett.* **117** 107401
- [14] Zhao D 2018 *Phys. Rev. A* **98** 033834
- [15] Zhao D, Gu Y, Chen H, Ren J, Zhang T and Gong Q 2015 *Phys. Rev. A* **92** 033836
- [16] Ridolfo A, Di Stefano O, Fina N, Saija R and Savasta S 2010 *Phys. Rev. Lett.* **105** 263601
- [17] Kewes G, Binkowski F, Burger S, Zschiedrich L and Benson O 2018 *ACS Photonics* **5** 4089
- [18] Hughes S, Richter M and Knorr A 2018 *Opt. Lett.* **43** 1834
- [19] Tamascelli D, Smirne A, Huelga S and Plenio M 2018 *Phys. Rev. Lett.* **120** 030402
- [20] Scully M and Zubairy M 1997 *Quantum Optics* (London: Cambridge University Press)
- [21] Cohen-Tannoudji C, Dupont-Roc J and Grynberg G 1998 *Atom-Photon Interactions: Basic Processes and Applications* (New York: Wiley)
- [22] Ding S, Li X, Nan F, Zhong Y T, Zhou L, Xiao X, Wang Q Q and Zhang Z 2017 *Phys. Rev. Lett.* **119** 177401
- [23] Guarnieri G, Smirne A and Vacchini B 2014 *Phys. Rev. A* **90** 022110
- [24] Ban M, Kitajima S and Shibata F 2018 *Phys. Rev. A* **97** 052101
- [25] Van Vlack C, Kristensen P and Hughes S 2012 *Phys. Rev. B* **85** 075303
- [26] Novotny L and Hecht B 2012 *Principles of Nano-Optics* 2nd edn (London: Cambridge University Press)
- [27] Kewes G, Herrmann K, Rodríguez-Oliveros R, Kuhlicke A, Benson O and Busch K 2017 *Phys. Rev. Lett.* **118** 237402
- [28] Dong Z C et al 2009 *Nat. Photon.* **4** 50
- [29] Johansson J, Nation P and Nori F 2013 *Comput. Phys. Commun.* **184** 1234
- [30] Johansson J, Nation P and Nori F 2012 *Comput. Phys. Commun.* **183** 1760
- [31] Gruner T and Welsch D 1996 *Phys. Rev. A* **53** 1818
- [32] Dung H, Knöll L and Welsch D 1998 *Phys. Rev. A* **57** 3931
- [33] Lu Y W, Li L Y and Liu J F 2018 *Sci. Rep.* **8** 7115